Pressure-induced electronic delocalization and superconductivity in $GaNb_4Se_8$

Yuejian Wang,[1,*] Zhongyan Wu,[2] Bhupendra K C,[3] Dongzhou Zhang,[4] Lin Wang,[2] Sanjay V. Khare,[3] Lilian Prodan,[5,6] and Vladimir Tsurkan[5,6]

[1]*Department of Physics, Oakland University, Rochester, Michigan 48309, USA*
[2]*Center for High-Pressure Science (CHiPS), State Key Laboratory of Metastable Materials Science and Technology, Yanshan University, Qinhuangdao, Hebei 066004, China*
[3]*Department of Physics and Astronomy, and Wright Center for Photovoltaics Innovation and Commercialization (PVIC), University of Toledo, Toledo, Ohio 43606, USA*
[4]*GeoSoilEnviroCARS, University of Chicago, Argonne, Illinois 60439, USA*
[5]*Experimental Physics V, Center for Electronic Correlations and Magnetism, University of Augsburg, 86135 Augsburg, Germany*
[6]*Institute of Applied Physics, Moldova State University, MD-2028 Chisinau, Republic of Moldova*

(Received 30 March 2026; revised 3 July 2026; accepted 19 August 2026; published 4 September 2026)

Understanding how electronic transport evolves from localized to itinerant regimes in correlated cluster solids remains an important challenge in condensed-matter physics. Here, we investigate the pressure-dependent transport properties of the lacunar spinel $GaNb_4Se_8$, a cluster Mott insulator at ambient conditions. At ambient pressure, the resistivity follows Efros-Shklovskii variable-range hopping, indicating Coulomb gap–controlled carrier localization. A pressure-induced electronic delocalization process begins at low pressures (∼5 GPa), as evidenced by the continuous suppression of room-temperature resistance. Upon further compression, the system undergoes a broad insulator-to-metal-like crossover in low-temperature transport, culminating in a fully metallic-like ground state at ∼17–18 GPa. In contrast, the crystallographic transition from the cubic phase to the monoclinic $C2$ phase starts at ∼20 GPa and ends near ∼32 GPa, demonstrating that the pressure-induced electronic evolution is completed before the onset of long-range structural symmetry breaking. At higher pressures, superconductivity (with a superconducting coherence length $\xi(0) \approx 80$–90 Å) emerges from a pressure-induced metallic-like regime. These results establish $GaNb_4Se_8$ as a platform for studying correlation-driven evolution of electronic transport in cluster-based solids.

DOI: 10.1103/8b8c-2wm3

I. INTRODUCTION

The Mott metal-insulator transition (MIT) represents a fundamental paradigm in condensed matter physics, where the competition between on-site Coulomb repulsion (U) and electronic bandwidth (W) governs the emergence of exotic quantum phases [1,2]. In many correlated electron systems, superconductivity emerges from the collapse of a Mott insulating state through external tuning parameters such as chemical doping or physical pressure [3]. While the macroscopic evolution of these phases is well documented, the microscopic structural mechanisms—specifically how local orbital degrees of freedom drive the electronic delocalization required for superconductivity—remain a subject of intense investigation [4].

Lacunar spinels with the general formula AM_4X_8 (A = Ga, Ge; M = V, Nb, Ta, Mo; and X = S, Se) offer a unique platform to explore these dynamics. Their crystal structure consists of molecular-like M_4 clusters, where electronic states are inherently localized within tetrahedral units [5–11]. The profound coupling between lattice and electronic degrees of freedom in these materials is often mediated by the Jahn-Teller (JT) effect, which lowers the local symmetry to stabilize the cluster Mott insulating state [5,6,12–16]. Among this family, $GaNb_4Se_8$ is of particular interest due to its narrow-gap insulating state and high sensitivity to compression [17]. Authors of previous high-pressure studies have revealed pressure-induced superconductivity in $GaNb_4Se_8$ and related lacunar spinels and suggested that the reduction of the MSe_6 octahedral distortion plays an important role in the emergence of superconductivity [18,19]. However, despite these pioneering studies, the microscopic mechanism underlying the transition from a localized to a superconducting state, as well as the interplay between lattice symmetry breaking and electronic reconstruction, remains elusive.

In this paper, we report the emergence of pressure-induced superconductivity in single-crystalline $GaNb_4Se_8$ and identify the underlying high-pressure structural framework. High-pressure synchrotron x-ray diffraction (XRD) reveals a crystal structural transition near 20 GPa. While significant peak broadening and sample pulverization under extreme compression pose challenges for definitive refinement, a monoclinic $C2$ model provides consistent identification of this previously unknown phase. Electrical transport measurements reveal a pressure-driven crossover from Efros-Shklovskii (ES) variable-range hopping (VRH) to a metallic-like regime, culminating in a zero-resistance superconducting state above 30 GPa ($T_c > 5$ K at 48.3 GPa). Our analysis reveals that the pressure-induced suppression of JT distortions acts as an

*Contact author: ywang235@oakland.edu

orbital gate, unlocking the localized Nb 4*d* states to facilitate electronic delocalization and bandwidth broadening. These results link the restoration of local symmetry to the Mott insulator-to-superconductor transition and identify the structural precursor to emergent quantum phases in $GaNb_4Se_8$.

II. METHODS

A. Synthesis and characterization

Single crystals of $GaNb_4Se_8$ (Fig. S1(a) in the Supplemental Material [20] including Refs. [21–24]) were grown from polycrystalline precursors prepared by a conventional solid-state reaction using high-purity elements: gallium pellets (99.9999%, Alfa Aesar), niobium powder (325 mesh, 99.8%, Alfa Aesar), and selenium granules (2–4 mm, 99.999%, ChemPUR). Stoichiometric mixtures of these elements were pressed into pellets, sealed under vacuum ($\sim 10^{-3}$ mbar) in double quartz ampoules, with the inner ampoule carbon-coated to prevent reactions between the sample and quartz. The sealed ampoules were heated in a muffle furnace according to the following sequence: ramped at 100 °C/h to 600 °C and held for 10 h; then ramped at 20 °C/h to 700 °C (dwelling for 20 h), 20 °C/h to 800 °C (25 h dwell), and finally, 10 °C/h to 900 °C with a 68 h dwell before cooling to room temperature at 100 °C/h.

After the first sintering cycle, phase analysis was performed using a STOE Stadi P diffractometer with Cu Kα radiation. The diffraction pattern revealed a predominant $GaNb_4Se_8$ phase with minor traces ($<10\%$) of hexagonal $NbSe_2$ impurity (Fig. S1(b) in the Supplemental Material) [20,25]. The product was subsequently reground, repelletized, and annealed again at 900 °C for an additional 72 h. The second cycle yielded a phase-pure $GaNb_4Se_8$ (Figs. S1(b) and S1(c) in the Supplemental Material [20]).

Single crystals were grown by the chemical vapor transport method using the as-synthesized polycrystalline material as a precursor. Approximately 2 g of $GaNb_4Se_8$, together with 0.2 g of iodine (as a transport agent) and 100 mg of selenium granules (to maintain stoichiometry), were sealed in an evacuated quartz ampoule (18 × 130 mm). Crystal growth was conducted in a temperature gradient between 1000 °C (hot zone) and 960 °C (cold zone) for ∼12 weeks, which was necessary for complete mass transport. The process yielded high-quality single crystals of well-defined cubic morphology with shiny (111) and (001) facets (Fig. S1(a) in the Supplemental Material [20]) as well as hexagonal platelike crystals formed in the cold zone.

The phase purity and elemental composition of the single crystals were examined using a ZEISS Crossbeam 550 scanning electron microscope equipped with energy-dispersive x-ray spectroscopy. The cubic crystals exhibited homogeneous single-phase composition (Fig. S1(d) in the Supplemental Material [20]) with an average stoichiometry of $Ga_{1.05(2)}Nb_4Se_{8.01(4)}$, assuming full Nb-site occupancy. The hexagonal plates were identified as $NbSe_2$ slightly doped with Ga (∼0.07%).

Magnetic susceptibility (χ) was measured using a Quantum Design MPMS 3 SQUID magnetometer on a larger single crystal from the same batch, with a magnetic field of 7 T applied along the [001] direction (Fig. S1(e) in the Supplemental Material [20]), in excellent agreement with previous studies [12,16,26].

B. High-pressure powder XRD

High-pressure XRD experiments were performed using a symmetric diamond anvil cell (DAC) equipped with 300 μm culets. Powder samples were loaded into a hole (serving as the sample chamber) with a diameter of 130 μm and a depth of ∼45 μm, drilled at the center of a rhenium gasket preindented by diamond anvils. A ruby sphere (<15 μm in diameter) was placed near the sampling material in the chamber for pressure determination [27].

High-pressure powder XRD (PXRD) experiments were conducted at 13-BM-C beamline of GSECARS [28]. The beamline was calibrated using a LaB_6 standard to determine the sample-to-detector distance and detector tilt angle.

After the beamline calibration, an initial XRD pattern was collected under ambient conditions to evaluate the crystal structure and sample quality. To minimize nonhydrostatic effects during measurements, helium gas was loaded using the gas-loading system at GSECARS (Argonne National Laboratory), serving as the pressure-transmitting medium to ensure quasihydrostatic conditions [21]. During the subsequent sealing of the chamber with helium gas, the pressure was maintained as low as possible (below 1 GPa) to enable data collection from the lowest attainable pressure point.

Pressure was increased using a membrane-driven system which significantly improved the efficiency and accuracy of the measurement. Upon reaching each target pressure, the DAC was stabilized for approximately 10 min to allow the sample to reach a quasiequilibrium state. Immediately after the 10 min relaxation period, the sample pressure was measured, and the XRD pattern was recorded. The pressure was then remeasured immediately after data acquisition, and the average of the two readings (before and after pattern collection) was taken as the effective sample pressure.

The collected diffraction rings were converted into conventional one-dimensional patterns (intensity vs 2θ) using DIOPTAS, allowing the evolution of diffraction features to be monitored in real time [29]. Subsequently, the XRD patterns were refined using GSAS-II to extract the lattice parameters and unit-cell volume at each pressure point [30]. Overall, two key phenomena were identified within the sample: the onset of a phase transition at approximately 20 GPa, which completed near 30 GPa, and the exceptional incompressibility inferred from equation-of-state analysis.

C. Electrical transport measurements

Electrical transport measurements under magnetic fields were performed using a cryogen-free C-Mag superconducting magnet system (Cryomagnetics, Inc.). For combined low-temperature and high-pressure measurements, a DAC equipped with 200 μm culets was employed. A Be–Cu gasket was preindented, and a ∼200-μm-diameter hole was drilled at the center of the indentation. The hole was filled with a cubic boron nitride (cBN)/epoxy insulating mixture and further compressed. A ∼120-μm-diameter hole was subsequently drilled to serve as the sample chamber. A single crystal of $GaNb_4Se_8$ (∼70 μm in diameter and ∼5 μm thick) was loaded together with NaCl as the pressure-transmitting medium and four platinum electrodes (∼2 μm thick). The electrodes were connected to Cu leads using Ag paste. Electrical resistance was measured in a standard four-probe configuration with an excitation current of 100 μA and a temperature sweep rate of 2 K/min.

Pressure was calibrated at room temperature using ruby fluorescence before cooling and after warming in each cycle, with a ∼5 μm ruby sphere positioned near the sample. Owing to thermal expansion of the DAC, cooling typically induced a pressure increase of ∼1 GPa; the pressure measured after warming was therefore used as the effective value. Representative $R(T)$ curves (Fig. S2 in the Supplemental Material [20]) show mild cooling-warming hysteresis. Data acquired during controlled warming (2 K/min) are smoother and less sensitive to thermal pressure drift, suggesting that pressure variations do not significantly affect the determination of superconducting transition temperatures.

D. Computational methods

Density functional theory (DFT) calculations were performed using VASP [31–33]. The Perdew-Burke-Ernzerhof [34] generalized gradient approximation (GGA) exchange-correlation functional was employed within the projector augmented-wave (PAW) framework [32,35,36]. Nb_sv, Ga_d, and Se PAW pseudopotentials were employed with a plane-wave cutoff energy of 520 eV. Brillouin zone sampling was performed using a $5 \times 5 \times 5$ k-point mesh, verified to be converged. Gaussian smearing with a width of 0.05 eV was applied to set the partial occupancies [37]. Structures were fully relaxed until the residual forces were below 0.01 eVÅ^{-1}, with an electronic self-consistency criterion of 10^{-6} eV.

The 0 GPa structure was obtained from the Materials Project database [38]. The high-pressure structure was obtained by relaxing the unit cell at the target pressure starting from the 0 GPa cubic phase. Optimized lattice parameters at 0 and 15 GPa are summarized in Table S1 in the Supplemental Material [20]. To account for correlation effects in Nb $4d$ states, DFT+U calculations were performed using an effective Hubbard parameter $U = 6$ eV, consistent with previous studies [18,39]. Hybrid-functional (HSE06) calculations were additionally carried out at ambient pressure to obtain an improved estimate of the electronic band gap. Due to the large unit cell (52 atoms), pressure-dependent electronic structure calculations were restricted to the GGA+U level.

Chemical bonding analysis was performed using the crystal orbital Hamilton population (COHP) method as implemented in the LOBSTER code [40–42]. Negative projected COHP(-pCOHP) analysis was carried out using a distance window of 2.5–4.5 Å to capture first-neighbor Nb–Se and Ga–Se interactions. Positive and negative −pCOHP values correspond to bonding and antibonding states, respectively, with the Fermi level set to 0 eV. Phonon calculations were performed using PHONOPY [43] to assess the thermodynamic stability of candidate crystal structures under pressure (see Table S2 in the Supplemental Material [20]).

III. RESULTS AND DISCUSSION

We first investigated the structural evolution of $GaNb_4Se_8$ under high pressure using synchrotron XRD [Fig. 1(a)]. At ambient pressure, sharp reflections can be indexed to a face-centered cubic (fcc) structure (space group $F\bar{4}3m$, $a = 10.42$ Å), a characteristic of lacunar spinels [8,14,18,19]. Upon compression, a structural transition onset was observed near 20 GPa, marked by the appearance of new reflections and the gradual weakening of the parent fcc peaks [Fig. 1(a)]. Above ∼32 GPa, the transformation to a high-pressure phase is complete. Notably, the recovered sample returns to the fcc phase upon decompression [Fig. 1(a), top], demonstrating the reversibility of this structural reconfiguration.

While single-crystal XRD was employed to investigate the pressure-induced structural transition, the intrinsic brittleness of $GaNb_4Se_8$ resulted in progressive crystal fragmentation upon compression [Note I and Figs. S3–S5 in the Supplemental Material [20]). Above ∼20 GPa, the crystal evolved into a multidomain and eventually powderlike state, leading to a substantial reduction in the number and quality of measurable single-crystal reflections. Concurrently, significant peak broadening and intensity redistribution developed at high pressure. These effects are consistent with contributions from crystallite strain, preferred orientation of fragmented crystallites, and increasing nonhydrostatic stress within the pressure chamber. Owing to the severe degradation of crystal quality and the limited number of measurable reflections, a reliable quantitative separation of these contributions is not possible. Nevertheless, the emergence of additional reflections that cannot be indexed within the parent $F\bar{4}3m$ symmetry provides direct evidence for pressure-induced symmetry lowering.

Consequently, guided by previous experimental and theoretical studies of lacunar spinels [9,10,44], we considered the two most physically motivated low-symmetry structural candidates, namely, orthorhombic $Imm2$ and monoclinic $C2$, for the high-pressure phase of this crystal. First-principles calculations indicate that the $Imm2$ structure is energetically less favorable [Fig. 1(b)], suggesting that the $C2$ model is more plausible from an energetic standpoint. However, due to the significant peak broadening and the limited number of resolvable reflections at high pressures, a reliable Rietveld refinement could not be performed. Instead, Le Bail fitting was carried out to test the consistency of the proposed $C2$ model with the experimental diffraction profiles [Fig. 1(c)]. The Le Bail analysis reproduces the observed diffraction pattern well and is consistent with the monoclinic $C2$ structural model, although it does not allow a unique structural determination. Therefore, the $C2$ structure is proposed as a plausible and internally consistent model for the high-pressure phase rather than a definitive structural assignment. As a representative example, the lattice parameters and x-ray reflections are listed in Table S3 in the Supplemental Material [20].

Following the identification of the high-pressure phase, we investigated the electronic transport properties of $GaNb_4Se_8$ under varied pressures and temperatures. As shown in Fig. 2(a), the resistance increases exponentially upon cooling at ambient pressure, a hallmark of carrier localization within the Nb_4 clusters driven by strong electron-electron correlations. While the transport is often phenomenologically

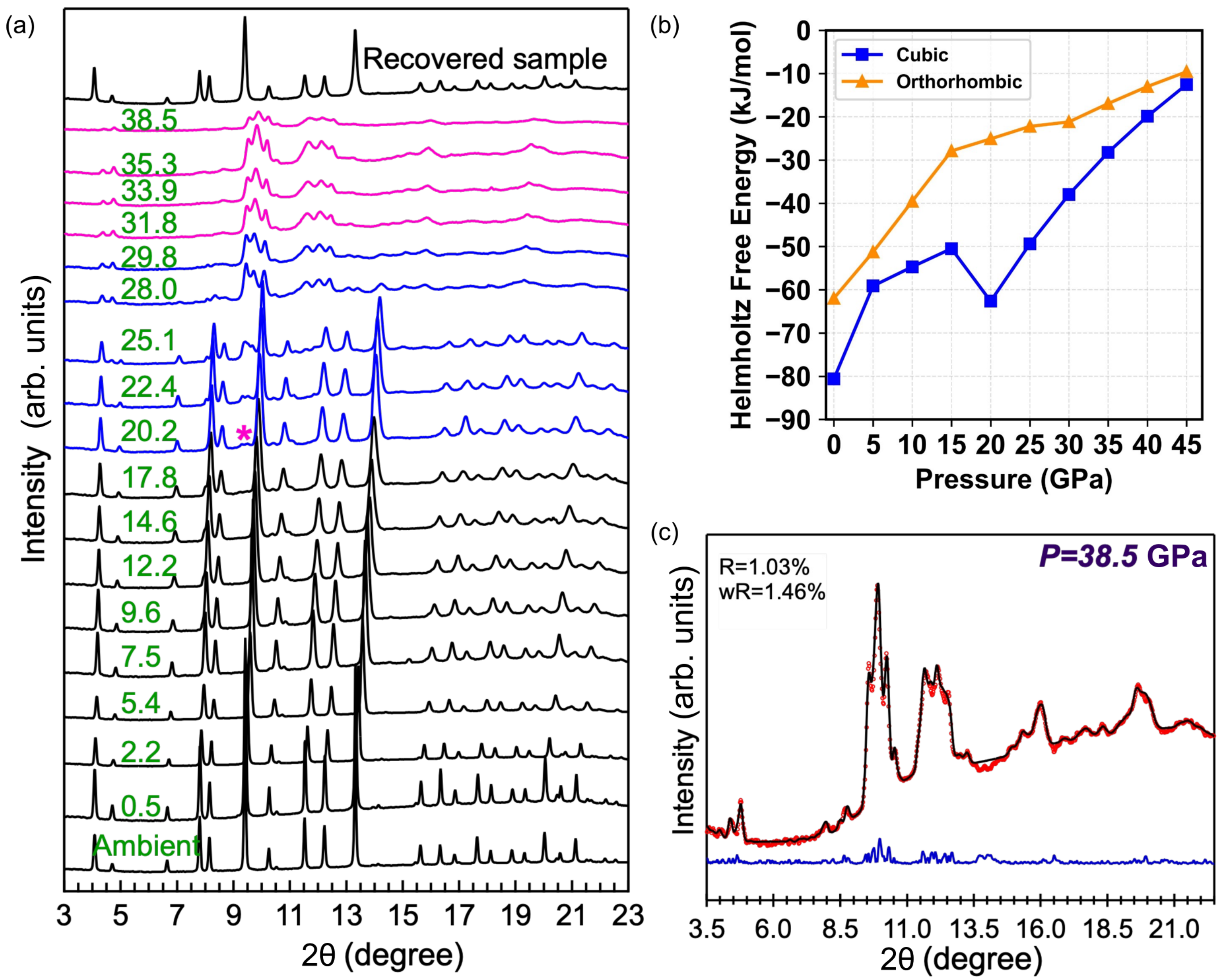

FIG. 1. Structural evolution of polycrystalline $GaNb_4Se_8$ under pressure. (a) Synchrotron XRD patterns collected upon compression from ambient conditions to 38.5 GPa and subsequent decompression (recovered sample). Pressures (in GPa) are indicated on the left. (b) Pressure dependence of calculated Helmholtz free energies for the cubic and orthorhombic structures. (c) Representative Le Bail refinement of diffraction pattern collected at 38.5 GPa. Red circles denote experimental data, black lines represent calculated profiles, and blue curves show the difference.

described by the Arrhenius activation law—yielding an activation energy of ∼146.7 meV in alignment with prior reports [16,19]—a more rigorous analysis reveals that the system is governed by the ES-VRH mechanism $\rho = \rho_0 e^{(\frac{T_0}{T})^{1/2}}$ [45] (Note II in the Supplemental Material [20]).

This model provides quantitative evidence for a fundamental transition in the localization state. In the high-temperature regime (220–300 K), the characteristic temperature $T_0 \approx$ 15 989.6 K corresponds to a localization length $\xi \approx 2.92$Å and a hopping energy of $WES \approx 87.9$ meV (at 260 K), suggesting that that the localization length is comparable with the bonding length in the Nb_4 cluster. However, upon cooling below 100 K, the hopping energy decreases to 75.3 meV (at 75 K) as carriers optimize for lower-energy paths, but T_0 increases significantly to ≈ 40 743.4 K. Consequently, ξ contracts sharply to ∼1.15 Å, aligning strikingly with the atom sites. This represents direct transport evidence for a localization-length contraction where carriers become strictly confined within individual Nb_4 tetrahedra, confirming GaN_b4Se_8 as a robust cluster Mott insulator.

The pressure-dependent resistance at room temperature [Fig. 2(b)] exhibits a pronounced decrease below ∼5 GPa, consistent with enhanced intercluster electronic overlap. Between 10 and 14 GPa, the pressure dependence of the resistance becomes progressively weaker, indicating a continuous crossover toward an electronically more delocalized state driven by pressure-induced bandwidth enhancement. Notably, this electronic crossover occurs well below the cubic-to-monoclinic structural transition (∼20–32 GPa) observed by XRD, suggesting that pressure-induced bandwidth enhancement within the cubic phase plays a dominant role in governing the evolution of electronic transport rather than being triggered by the onset of long-range structural symmetry breaking.

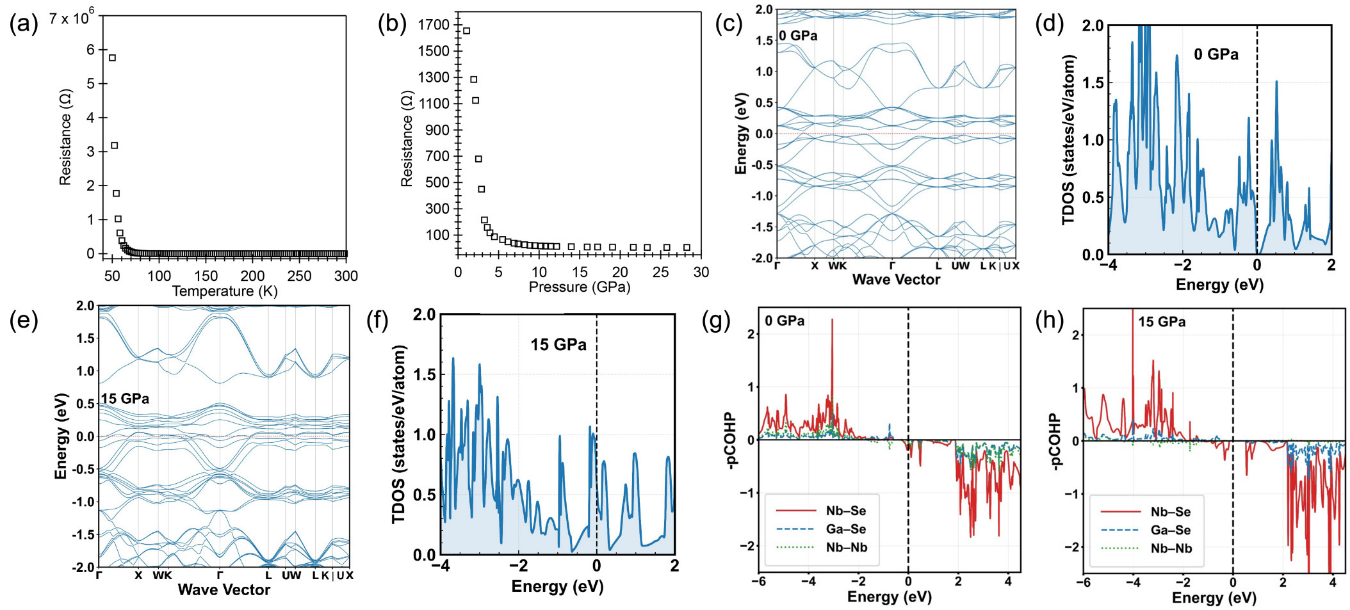

FIG. 2. Pressure-driven electronic evolution in $GaNb_4Se_8$. (a) Temperature-dependent resistance at ambient pressure. (b) Pressure dependence of resistance at room temperature. (c) and (d) Electronic band structure and density of states (DOS) of cubic $GaNb_4Se_8$ at 0 GPa. (e) and (f) Electronic band structure and DOS at 15 GPa. (g) and (h) –pCOHP for selected Nb–Se, Ga–Se, and Nb–Nb nearest-neighbor interactions at 0 and 15 GPa. Positive and negative –pCOHP values correspond to bonding and antibonding contributions, respectively. The Fermi level is set to 0 eV.

To understand the microscopic origin of the observed transport behavior and the pressure-induced metallization, density-functional calculations were performed. At ambient pressure, the calculated band structure [Fig. 2(c)] and total density of states [Fig. 2(d)] reveal a narrow energy gap separating the valence and conduction bands, aligning with the observed cluster Mott characteristics of $GaNb_4Se_8$. Crucially, the states near the Fermi level (E_F) are dominated by Nb_4 cluster molecular orbitals, providing a theoretical basis for the carrier localization observed in transport. The electronic configuration obtained from DFT calculations provides a microscopic foundation for the localization-length contraction inferred from our ES-VRH analysis. While the experimental transport captures the temperature-dependent evolution of carrier localization, the computational ground state (0 K) reveals that the states near E_F are inherently confined within individual Nb_4 clusters. This spatial confinement, enforced by strong electron correlations, reflects the evolution from a relatively delocalized electronic state at high temperatures toward a more localized state at low temperatures.

Under compression, the electronic bands broaden significantly and approach the Fermi level ∼15 GPa [Fig. 2(e)], accompanied by a finite density of states at E_F [Fig. 2(f)]. Notably, these calculations are performed within the cubic symmetry, indicating that pressure-driven bandwidth enhancement leads to a reduction of the effective U/W ratio and thus promotes electronic delocalization within the cubic phase. Here, U and W denote the on-site Coulomb interaction and the electronic bandwidth, respectively. This provides a qualitative framework for understanding the pressure-induced evolution toward metallic-like behavior, consistent with the experimental observation that electronic delocalization occurs within the cubic structural framework prior to the emergence of the long-range monoclinic phase.

To further elucidate this evolution, we performed –pCOHP calculations [Figs. 2(g)–2(h)]. At ambient pressure, the average integrated COHP for Nb–Se bonds is −0.88 eV per bond, whereas Ga–Se bonds contribute only −0.013 eV per bond, confirming that the electronic states near E_F are primarily governed by Nb–Se bonding interactions, while the contribution from Ga–Se bonds is negligible.

Under compression, distinct antibonding features emerge below the Fermi level near −0.5 eV [Fig. 2(h)], accompanied by a progressive reduction in the Nb–Se bonding strength. Quantitatively, the average integrated COHP (ICOHP) for Nb–Se bonds decreases in magnitude from −0.88 eV per bond at ambient pressure to −0.72 eV at 15 GPa, representing a reduction of approximately 15%. Consistently, the total ICOHP summed over all bonding interactions becomes less negative with increasing pressure, evolving from −0.35 eV at 0 GPa to −0.21 eV at 15 GPa. This pressure-induced weakening of the Nb–Se bonding strength reflects a transition from rigid, covalentlike carrier confinement within the Nb_4 clusters toward a more delocalized regime. By facilitating enhanced intercluster electronic hopping, this redistribution of bonding states drives the broadening of the Nb 4d bandwidth, ultimately triggering the collapse of the Mott insulating state and the emergence of the metallic-like state observed in our transport measurements.

To identify the structural origin of this pressure-induced delocalization, we investigated the evolution of the local coordination environment, specifically the $NbSe_6$ octahedra that constitute the Nb_4 clusters [Figs. 3(a)–3(d)]. At ambient pressure, the Nb atoms are significantly displaced from the centrosymmetric position of the $NbSe_6$ octahedron, as evidenced

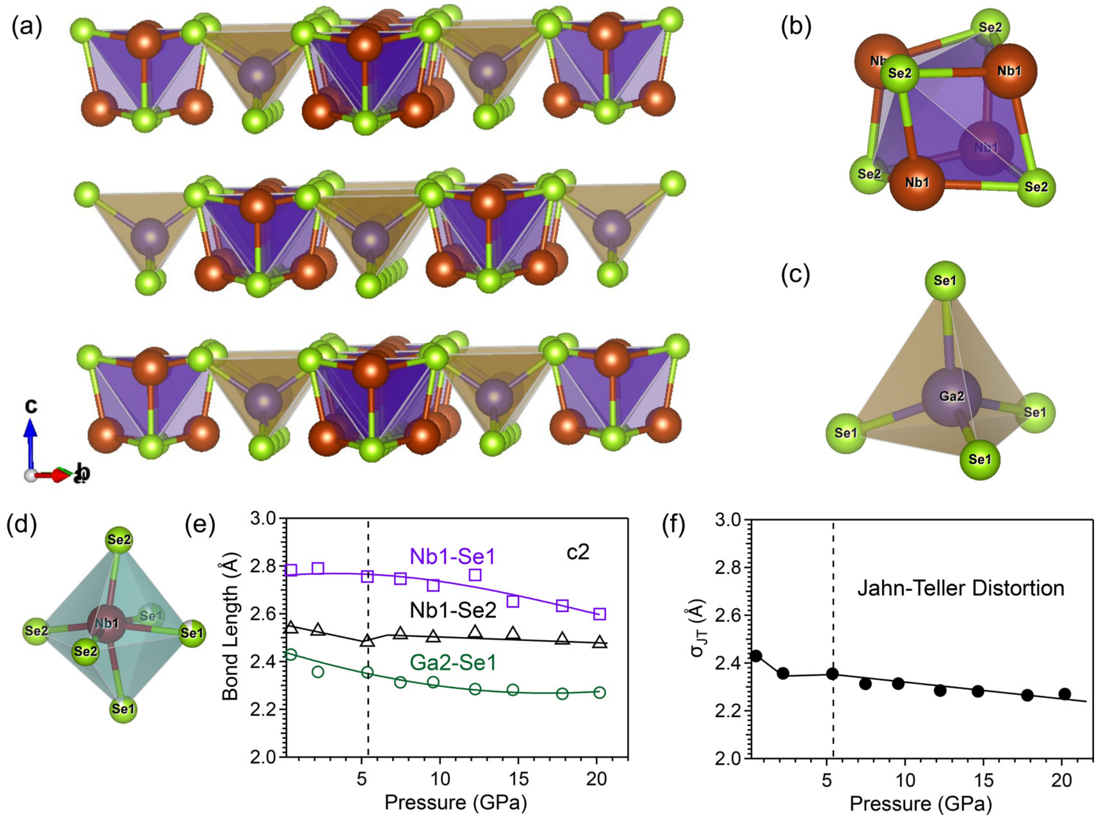

FIG. 3. Pressure-driven modification of local bonding in $GaNb_4Se_8$. (a) Crystal structure of $GaNb_4Se_8$, composed of Nb_4Se_4 clusters and $GaSe_4$ tetrahedra. (b) and (c) Local structural units highlighting the Nb_4Se_4 cluster and $GaSe_4$ tetrahedron, respectively. (d) Schematic representation of the $NbSe_6$ octahedral coordination environment. (e) Pressure dependence of selected Nb–Se and Ga–Se bond lengths obtained from Rietveld refinement of synchrotron XRD data. (f) Evolution of the JT distortion parameter as a function of pressure.

by the inequivalent Nb (1)–Se(1) and Nb(1)–Se(2) bond lengths [Fig. 3(e)]. This structural asymmetry is a manifestation of a JT distortion, which serves to split the Nb 4*d* orbitals and stabilize the localized Mott insulating state. Our analysis reveals a distinct two-regime evolution of these bond lengths under compression. Below ∼5 GPa, the Nb(1)–Se(2) bond contracts linearly, while the Nb(1)–Se(1) bond remains nearly constant, indicating a progressive shift of the Nb atom within the octahedron. However, above ∼5 GPa, this trend reverses: The Nb(1)–Se(2) bond becomes pressure independent, while the Nb(1)–Se(1) bond undergoes significant compression.

This crossover is quantitatively captured by the JT distortion parameter σ_{JT} defined as [46–48]

$$\sigma_{JT} = \left\{ \sum_{i=1}^{2} \left(L_{Nb(1)-Se(i)} - \bar{L}_{Nb-Se} \right)^2 \right\}^{1/2},$$

where $L_{Nb(1)-Se(i)}$ denotes the specific bond lengths between Nb and Se atoms, and $\bar{L}_{Nb-Se}$ represents the average Nb−Se bond length within the $NbSe_6$ octahedron. While σ_{JT} remains nearly constant in the low-pressure regime, it exhibits a progressive decrease above 5 GPa, signaling the suppression of the structural distortion and a move toward a more centrosymmetric Nb coordination [Fig. 3(f)]. Crucially, this structural crossover at ∼5 GPa coincides precisely with the onset of the insulator-to-metal transition and the rapid decline in resistance observed in our transport measurements. The pressure-induced suppression of the JT distortion provides the structural basis for the redistribution of bonding states revealed by our –pCOHP analysis. By restoring local symmetry, compression effectively reduces the orbital splitting and facilitates enhanced overlap between the Nb 4*d* orbitals of neighboring clusters. This structural unlocking drives the expansion of the localization length (ξ) and the broadening of the bandwidth, ultimately overcoming the on-site Coulomb repulsion to trigger the collapse of the Mott state. Consequently, the JT effect in $GaNb_4Se_8$ acts as the primary orbital gate controlling the transition from rigid, cluster-bound carrier confinement to a fully delocalized, metallic-like regime.

Temperature-dependent resistance measurements further clarify the pressure-driven electronic evolution [Fig. 4(a)]. At low pressures, the resistance increases steeply upon cooling, characteristic of a Mott insulating state where carriers are strictly confined within Nb_4 clusters. With increasing pressure, the temperature dependence gradually weakens and transitions to a metallic-like regime between 10 and 14 GPa, confirming a pressure-induced insulator–metallic-like transition. In contrast with the ES-VRH behavior observed at ambient pressure, the resistance curves under compression systematically deviate from standard hopping models. This deviation suggests the emergence of metallic-like channels interwoven with thermally activated transport as the system approaches the metallic-like regime.

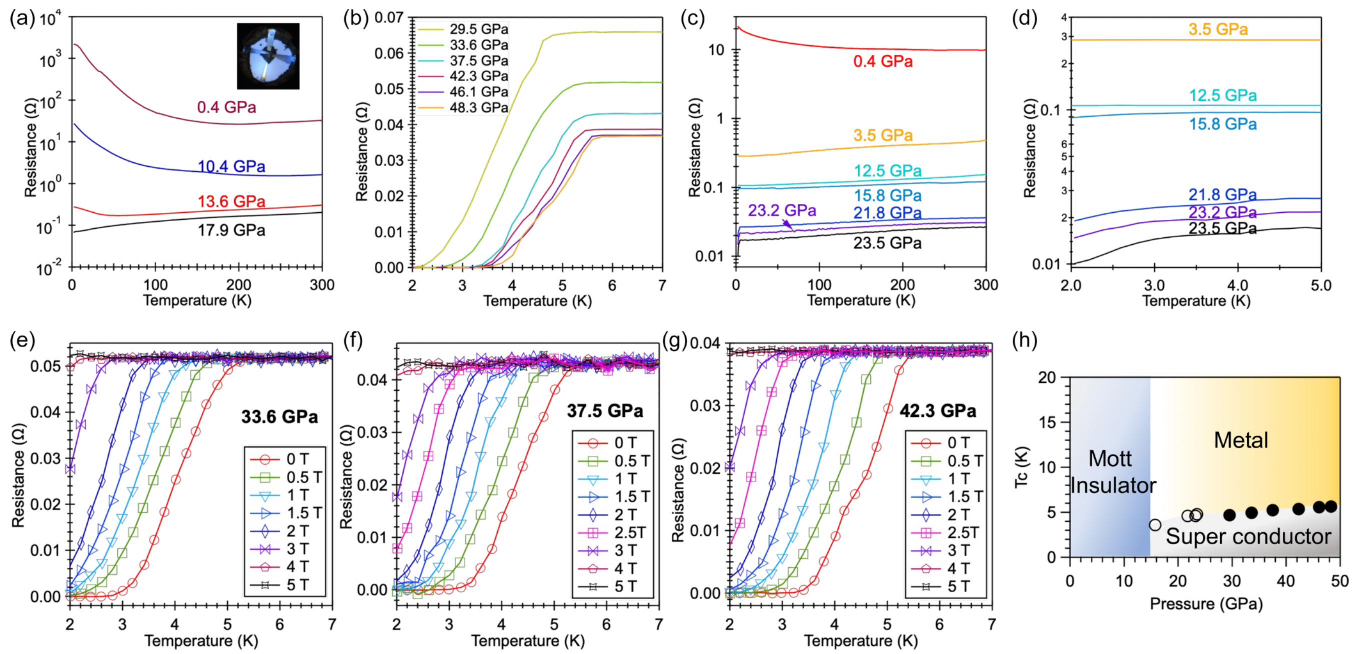

FIG. 4. Pressure-induced superconductivity in single-crystalline $GaNb_4Se_8$. The magnetic-field orientation relative to the crystallographic axes was not recorded during the measurements. (a) Temperature dependence of the electrical resistance under applied pressure. Inset: Schematic of the electrode configuration in the DAC. (b) Low-temperature resistance highlighting the emergence of superconductivity at high pressures. (c) Temperature-dependent resistance upon pressure release (decompression). (d) Enlarged view of the superconducting transition shown in (c). (e)–(g) Magnetic-field dependence of the superconducting transition at representative pressures. (h) Pressure–temperature phase diagram summarizing the evolution from a Mott insulating state through a broad crossover regime with gradually decreasing resistance and partial metallic behavior, culminating in a metallic-like state and superconductivity at higher pressures. Solid (open) symbols represent transition temperatures obtained during compression (decompression).

In the intermediate crossover region (10–14 GPa), where traditional thermal activation and hopping models fail to provide a consistent fit, the resistance curves are well described by an empirical for $R(T) = R_0 + Ae^{-Bt}$, here, the parameter B acts as a thermal sensitivity coefficient, reflecting the degree of carrier confinement within the Nb_4 network. As pressure increases, B exhibits a systematic and dramatic reduction (0.0447 and 0.000 79 K^{-1} at 10.4 and 13.6 GPa, respectively).

Physically, this attenuation of B quantifies the progressive softening of the Mott insulating state. As the JT distortion is suppressed ($\sigma_{JT} \downarrow$) and the Nb 4d bandwidth (W) broadens, the energy barrier for intercluster hopping diminishes. Consequently, the resistance becomes increasingly insensitive to temperature fluctuations, signaling that the localization length is expanding beyond individual Nb_4 clusters. When B approaches its minimum value at 13.6 GPa, the inferred increase in localization length suggests that electronic states become progressively more delocalized, facilitating the crossover toward metallic-like transport and ultimately superconductivity at higher pressures.

At higher pressures, a sharp drop in resistance appears upon cooling, reaching a zero-resistance state between 29.5 and 48.3 GPa [Fig. 4(b)]. The superconducting transition temperature T_c increases monotonically with pressure, exceeding 5 K at 48.3 GPa. The emergence of a robust zero-resistance state is consistent with pressure-enhanced bandwidth and strengthened intercluster coupling, which promote long-range phase coherence. Notably, the robust zero-resistance superconducting state observed in the present single-crystal measurements emerges near 30 GPa, substantially higher than the ∼13 GPa superconducting behavior previously reported for polycrystalline samples [19], where a magnetic field–sensitive resistance drop was observed without reaching zero resistance. In the present work, partial resistance drops are also detected at 17.9, 21.5, and 26.1 GPa (Fig. S6 in the Supplemental Material [20]), preceding the establishment of a zero-resistance state. The difference between the previous polycrystalline measurements and the present single-crystal results may reflect differences in sample morphology, pressure-transmitting medium, current pathways, strain conditions, pressure calibration, or measurement configuration. Further investigation is required to clarify the origin of this discrepancy.

The intrinsic nature of the electronic reconstruction in $GaNb_4Se_8$ is further evidenced by the reversibility of the observed transitions. Upon decompression [Figs. 4(c) and 4(d)], the superconducting state gradually weakens and vanishes near ∼12 GPa with the insulating behavior eventually reappearing at ambient pressure. This recovery indicates that the Mott-to-superconductor transition originates from an intrinsic electronic reconfiguration rather than irreversible structural damage, consistent with the restoration of the cubic symmetry upon pressure release. Notably, the transition pressures exhibited a pronounced hysteresis (∼30 GPa during compression vs ∼12 GPa during decompression), a common feature in pressure-tuned correlated systems.

Magnetic field–dependent resistance measurements [Figs. 4(e)–4(g)] confirm the high-pressure phase as a characteristic type-II superconductor. The superconducting transition is progressively suppressed with increasing magnetic field, and the upper critical field $\mu_0 H_{c2}(T)$ was analyzed using both the Ginzburg-Landau (GL) [49] and Werthamer-Helfand-Hohenberg (WHH) [50] models. Within the GL formalism, the temperature dependence is described by

$$\mu_0 H_{c2}(T) = \mu_0 H_{c2}(0)\frac{1-(T/T_c)^2}{1+(T/T_c)^2},$$

while the WHH model in the dirty limit provides

$$\mu_0 H_{c2}(0) = -0.693 T_c \frac{d(\mu_0 H_{c2})}{dT}\bigg|_{T=T_c}.$$

The zero-temperature upper critical field $\mu_0 H_{c2}(0)$ was estimated between 4.26 and 5.18 T across the 33.6–42.3 GPa range (Fig. S7 and Table S4 in the Supplemental Material for data fitting and data summary, respectively [20]). The resulting superconducting coherence length $\xi(0)$, calculated via $\mu_0 H_{c2}(0) = \frac{\Phi_0}{2\pi\xi^2(0)}$, where $\Phi_0 = 2.07 \times 10^{-15}$ Wb, is approximately 8–9 nm. It is important to note that this $\xi(0)$ represents the spatial extent of the Cooper pairs in the delocalized metallic-like state, which is significantly larger than the electronic localization length observed in the Mott insulating phase at low pressures.

The Pauli paramagnetic limit $H_P \approx 1.84 T_c \approx 9-10$ T remains significantly higher than the measured $\mu_0 H_{c2}(0)$, indicating that the upper critical field is primarily governed by orbital pair breaking. The slight increase in $\xi(0)$ with pressure may reflect the continued evolution of electronic correlations and the further broadening of the Nb 4*d* bandwidth.

The synthesized electronic phase diagram of $GaNb_4Se_8$ [Fig. 4(h)] reveals a sequential evolution: from a cluster Mott insulator governed by JT-induced confinement at ambient pressure, through a metallic-like regime characterized by the suppression of σ_{JT}, and finally, to a robust superconducting state. This pressure-temperature–tuned progression highlights the delicate interplay between local structural distortions and long-range electronic order in cluster-based Mott systems.

In summary, in this study, we establish the emergence of pressure-induced superconductivity within a monoclinic *C*2 framework in single-crystalline $GaNb_4Se_8$. By utilizing high-quality single crystals, we identify the structural foundation for the transition from highly confined, cluster-bound carriers to a delocalized superconducting state.

Microscopically, we demonstrate that the pressure-induced suppression of JT distortions acts as a critical orbital gate. This structural unlocking drives the expansion of the localization length ξ, facilitating the intercluster electronic overlap necessary for long-range phase coherence. Our results link the restoration of local symmetry to the collapse of the Mott state, identifying the orbital gate as a primary driver for overcoming electron correlations in cluster-based quantum materials.

ACKNOWLEDGMENTS

We acknowledge the support of GeoSoilEnviroCARS(Sector 13), which is supported by the National Science Foundation (NSF)−Earth Sciences (Grant No. EAR-1634415). In this research, we used resources of the Advanced Photon Source, a U.S. Department of Energy (DOE) Office of Science User Facility operated for the DOE Office of Science by Argonne National Laboratory under Contract No. DE-AC02-06CH11357. Use of the COMPRES-GSECARS gas-loading system and 13-BM-C was supported by COMPRES under NSF Cooperative Agreement No. EAR-1661511 and by GSECARS through NSF Grant No. EAR-1634415 and DOE Grant No. DE-FG02-94ER14466. L.W. acknowledges the support by the Natural Science Foundation of China (Grants No. 52288102 and No. 52090020) and the support from the S&T Program of Hebei (Grant No. 225A1102D). L.P. and V.T. acknowledge the support of the Deutsche Forschungsgemeinschaft through Transregional Research Collaboration TRR 360 (Project No. 492547816) and by the project ANCD (cod 011201 Moldova). D.Z. acknowledges the support of NSF Grant No. EAR-2246686. Z.W. acknowledges the support from the Natural Science Foundation of China (Grant No. 52502334) and the support from the Hebei Natural Science Foundation (Grant No. E2025203044). Y.W. is grateful to the Faculty Research Grant from Oakland University for supporting this research.

DATA AVAILABILITY

There are no publicly available research data or software supporting this manuscript. Requests for further information or data should be sent to the authors.

[1] B. Keimer, S. A. Kivelson, M. R. Norman, S. Uchida, and J. Zaanen, From quantum matter to high-temperature superconductivity in copper oxides, Nature (London) **518**, 179 (2015).

[2] R. Yu and Q. Si, Mott transition in multiorbital models for iron pnictides, Phys. Rev. B **84**, 235115 (2011).

[3] M. Tinkham, *Introduction to Superconductivity* (McGraw-Hill, New York, 1975).

[4] X. J. Chen, V. V. Struzhkin, Z. Wu, M. Somayazulu, J. Qian, S. Kung, A. N. Christensen, Y. Zhao, R. E. Cohen, H.-k. Mao, *et al.*, Hard superconducting nitrides, Proc. Natl. Acad. Sci. USA **102**, 3198 (2005).

[5] V. Felea, P. T. Cong, L. Prodan, D. I. Gorbunov, T. Nomura, Y. Skourski, S. Zherlitsyn, J. Wosnitza, Z. Wang, A. Miyata, *et al.*, High-field phase transitions in the orbitally ordered multiferroic GeV_4S_8, Phys. Rev. B **101**, 064413 (2020).

[6] Á. Butykai, S. Bordács, I. Kézsmárki, V. Tsurkan, A. Loidl, J. Döring, E. Neuber, P. Milde, S. C. Kehr, and L. M. Eng, Characteristics of ferroelectric-ferroelastic domains in Néel-type skyrmion host GaV_4S_8, Sci. Rep. **7**, 44663 (2017).

[7] E. Ruff, A. Butykai, K. Geirhos, S. Widmann, V. Tsurkan, E. Stefanet, I. Kézsmárki, A. Loidl, and P. Lunkenheimer, Polar and magnetic order in GaV_4S_8, Phys. Rev. B **96**, 165119 (2017).

[8] L. Cario, B. Corraze, and E. Janod, Physics and chemistry of chalcogenide quantum materials with lacunar spinel structure, Chem. Mater. **37**, 532 (2025).

[9] Y. Wang, S. Rahman, E. Sun, C. Knill, D. Zhang, L. Wang, V. Tsurkan, and I. Kézsmárki, From semiconducting to metallic: Jahn-Teller-induced phase transformation in skyrmion host GaV_4S_8, J. Phys. Chem. C **125**, 5771 (2021).

[10] Y. Wang, Z. Shen, D. Zhang, L. Wang, V. Tsurkan, L. Prodan, A. Loidl, B. B. Dumre, and S. V. Khare, Pressure-induced changes in the crystal structure and electrical conductivity of GeV_4S_8, Chem. Mater. **36**, 3128 (2024).

[11] M. Magnaterra, J. Attig, L. Peterlini, M. Hermanns, M. H. Upton, J. Kim, L. Prodan, V. Tsurkan, I. Kézsmárki, P. H. M. van Loosdrecht, *et al.*, Quasimolecular $J_{\text{tet}} = 3/2$ moments in the cluster mott insulator $GaTa_4Se_8$, Phys. Rev. Lett. **133**, 046501 (2024).

[12] H. Ishikawa, T. Yajima, A. Matsuo, Y. Ihara, and K. Kindo, Nonmagnetic ground states and a possible quadrupolar phase in 4*d* and 5*d* lacunar spinel selenides GaM_4Se_8(M = Nb, Ta), Phys. Rev. Lett. **124**, 227202 (2020).

[13] K. Geirhos, J. Langmann, L. Prodan, A. A. Tsirlin, A. Missiul, G. Eickerling, A. Jesche, V. Tsurkan, P. Lunkenheimer, W. Scherer, *et al.*, Cooperative cluster Jahn-Teller effect as a possible route to antiferroelectricity, Phys. Rev. Lett. **126**, 187601 (2021).

[14] T.-H. Yang, T. Chang, Y.-S. Chen, and K. W. Plumb, Jahn-Teller driven quadrupolar ordering and spin-orbital dimer formation in $GaNb_4Se_8$, Phys. Rev. B **109**, 144101 (2024).

[15] J. Langmann, G. Eickerling, L. Prodan, A. A. Tsirlin, M. Winkler, S. Bordács, V. Tsurkan, and I. Kézsmárki, Atomic-scale polar helix in inorganic crystals, Chem. Mater. **36**, 11180 (2024).

[16] M. Winkler, L. Prodan, V. Tsurkan, P. Lunkenheimer, and I. Kézsmárki, Antipolar transitions in $GaNb_4Se_8$ and $GaTa_4Se_8$, Phys. Rev. B **106**, 115146 (2022).

[17] S. Reschke, F. Meggle, F. Mayr, V. Tsurkan, L. Prodan, H. Nakamura, J. Deisenhofer, C. A. Kuntscher, and I. Kézsmárki, Lattice dynamics and electronic excitations in a large family of lacunar spinels with a breathing pyrochlore lattice structure, Phys. Rev. B **101**, 075118 (2020).

[18] R. Pocha, D. Johrendt, B. Ni, and M. M. Abd-Elmeguid, Crystal structures, electronic properties, and pressure-induced superconductivity of the tetrahedral cluster compounds $GaNb_4S_8$, $GaNb_4Se_8$, and $GaTa_4Se_8$, J. Am. Chem. Soc. **127**, 8732 (2005).

[19] M. M. Abd-Elmeguid, B. Ni, D. I. Khomskii, R. Pocha, D. Johrendt, X. Wang, and K. Syassen, Transition from Mott insulator to superconductor in $GaNb_4Se_8$ and $GaTa_4Se_8$ under high pressure, Phys. Rev. Lett. **93** 126403 12 (2004).

[20] See Supplemental Material at http://link.aps.org/supplemental/10.1103/8b8c-2wm3 for high-pressure single-crystal XRD and technical details of transport analysis.

[21] M. Rivers, V. B. Prakapenka, A. Kubo, C. Pullins, C. M. Holl, and S. D. Jacobsen, The COMPRES/GSECARS gas-loading system for diamond anvil cells at the Advanced Photon Source, High Pressure Res. **28**, 273 (2008).

[22] G. Sheldrick, A short history of SHELX, Acta Crystallogr. Sect. A **64**, 112 (2007).

[23] O. V. Dolomanov, L. J. Bourhis, R. J. Gildea, J. A. K. Howard, and H. Puschmann, OLEX2: A complete structure solution, refinement and analysis program, J. Appl. Crystallogr. **42**, 339 (2009).

[24] R. Rösslhuber, R. Hübner, M. Dressel, and A. Pustogow, Pressure-dependent dielectric response of the frustrated Mott insulator k-$(BEDT\text{-}TTF)_2Ag_2(CN)_3$, Phys. Rev. B **107**, 075113 (2023).

[25] A. Meerschaut and C. Deudon, Crystal structure studies of the 3R-$Nb_{1.09}S_2$ and the 2H-$NbSe_2$ compounds: Correlation between nonstoichiometry and stacking type (= polytypism), Mater. Res. Bull. **36**, 1721 (2001).

[26] T. Petersen, L. Prodan, V. Tsurkan, H.-A. Krug von Nidda, I. Kézsmárki, U. K. Rößler, and L. Hozoi, How correlations and spin-orbit coupling work within extended orbitals of transition-metal tetrahedra of 4d/5d lacunar spinels, J. Phys. Chem. Lett. **13**, 1681 (2022).

[27] H. K. Mao, J. Xu, and P. M. Bell, Calibration of the ruby pressure gauge to 800 kbar under quasi-hydrostatic conditions, J. Geophys. Res.: Solid Earth **91**, 4673 (1986).

[28] D. Zhang, J. Xu, P. K. Dera, M. L. Rivers, P. J. Eng, V. B. Prakapenka, and J. E. Stubbs, Recent developments on high-pressure single-crystal x-ray diffraction at the Partnership for eXtreme Xtallography (PX2) program, Phys. Chem. Miner. **49**, 19 (2022).

[29] C. Prescher and V. B. Prakapenka, DIOPTAS: A program for reduction of two-dimensional x-ray diffraction data and data exploration, High Pressure Res. **35**, 223 (2015).

[30] B. H. Toby and R. B. Von Dreele, GSAS-II: The genesis of a modern open-source all purpose crystallography software package, J. Appl. Crystallogr. **46**, 544 (2013).

[31] G. Kresse and J. Furthmüller, Efficiency of *ab-initio* total energy calculations for metals and semiconductors using a plane-wave basis set, Comput. Mater. Sci. **6**, 15 (1996).

[32] G. Kresse and D. Joubert, From ultrasoft pseudopotentials to the projector augmented-wave method, Phys. Rev. B **59**, 1758 (1999).

[33] M. Sitaula, V. T. Barone, S. R. Kandel, B. KC, B. B. Dumre, R. J. Ellingson, and S. V. Khare, Optoelectronic and mechanical properties of antimony sulfide selenide ternary $Sb_2(S_xSe_{1-x})_3$ alloys using first principles methods, Comput. Condens. Matter **44**, e01103 (2025).

[34] J. P. Perdew, J. A. Chevary, S. H. Vosko, K. A. Jackson, M. R. Pederson, D. J. Singh, and C. Fiolhais, Atoms, molecules, solids, and surfaces: Applications of the generalized gradient approximation for exchange and correlation, Phys. Rev. B **46**, 6671 (1992).

[35] P. E. Blochl, Projector augmented-wave method, Phys. Rev. B **50**, 17953 (1994).

[36] N. J. Szymanski, I. Khatri, J. G. Amar, D. Gall, and S. V. Khare, Unconventional superconductivity in 3*d* rocksalt transition metal carbides, J. Mater. Chem. C **7**, 12619 (2019).

[37] D. Fang and Y. Li, Structural, electronic, and optical properties of ZnO: $ZnSnN_2$ compounds for optoelectronics and photocatalyst applications, Phys. Lett. A **384**, 126670 (2020).

[38] A. Jain, S. P. Ong, G. Hautier, W. Chen, W. D. Richards, S. Dacek, S. Cholia, D. Gunter, D. Skinner, G. Ceder, *et al.*, Commentary: The Materials Project: A materials genome approach to accelerating materials innovation, APL Mater. **1**, 011002 (2013).

[39] Y. Wang, D. Puggioni, and J. M. Rondinelli, Assessing exchange-correlation functional performance in the chalco-

genide lacunar spinels GaM_4Q_8 (M = Mo, V, Nb, Ta; Q = S, Se), Phys. Rev. B **100**, 115149 (2019).

[40] V. L. Deringer, A. L. Tchougréeff, and R. Dronskowski, Crystal orbital Hamilton population (COHP) analysis as projected from plane-wave basis sets, J. Phys. Chem. A **115**, 5461 (2011).

[41] S. Maintz, V. L. Deringer, A. L. Tchougréeff, and R. Dronskowski, Analytic projection from plane-wave and PAW wavefunctions and application to chemical-bonding analysis in solids, J. Comput. Chem. **34**, 2557 (2013).

[42] B. KC, V. T. Barone, S. R. Kandel, M. Sitaula, B. B. Dumre, R. J. Ellingson, and S. V. Khare, Computational investigation of structural, electronic, and optical properties of $(In_xGa_{1-x})_2O_3$ alloys as candidates for emitter layer application in solar cells, Physica B **715**, 417615 (2025).

[43] A. Togo and I. Tanaka, First principles phonon calculations in materials science, Scr. Mater. **108**, 1 (2015).

[44] H. Deng, J. Zhang, M. Y. Jeong, D. Wang, Q. Hu, S. Zhang, R. Sereika, T. Nakagawa, B. Chen, X. Yin, *et al.*, Metallization of quantum material $GaTa_4Se_8$ at high pressure, J. Phys. Chem. Lett. **12**, 5601 (2021).

[45] X. J. Chen, C. L. Zhang, J. S. Gardner, J. L. Sarrao, and C. C. Almasan, Variable-range-hopping conductivity of the half-doped bilayer manganite $LaSr_2Mn_2O_7$, Phys. Rev. B **68**, 064405 (2003).

[46] J. Ruiz-Fuertes, A. Friedrich, J. Pellicer-Porres, D. Errandonea, A. Segura, W. Morgenroth, E. Haussühl, C. Y. Tu, and A. Polian, Structure solution of the high-pressure phase of $CuWO_4$ and evolution of the Jahn-Teller distortion, Chem. Mater. **23**, 4220 (2011).

[47] P. Wang, S. C. Zhu, Y. Zou, H. Chen, Y. Liu, W. Li, J. Chen, J. Zhu, L. Wu, S. Wang, *et al.*, Concurrent pressure-induced spin-state transitions and Jahn-Teller distortions in MnTe, Chem. Mater. **34**, 3931 (2022).

[48] M. N. Sanz-Ortiz and F. Rodríguez, Photoluminescence properties of Jahn-Teller transition-metal ions, J. Chem. Phys. **131**, 124512 (2009).

[49] V. L. Ginzburg and L. D. Landau, On the Theory of Superconductivity, in *On Superconductivity and Superfluidity: A Scientific Autobiography*, edited by V. L. Ginzburg (Springer Berlin Heidelberg, Berlin, Heidelberg, 2009), pp. 113–137.

[50] N. R. Werthamer, E. Helfand, and P. C. Hohenberg, Temperature and purity dependence of the superconducting critical field, H_{c2}. III. Electron spin and spin-orbit effects, Phys. Rev. **147**, 295 (1966).